Materials Horizons

COMMUNICATION

View Article Online
View Journal | View Issue

Cite this: *Mater. Horiz.*, 2020, 7, 530

Received 29th August 2019,
Accepted 14th October 2019

DOI: 10.1039/c9mh01371g

rsc.li/materials-horizons

Highly stable and spectrum-selective ultraviolet photodetectors based on lead-free copper-based perovskites†

Ying Li,[a] Zhifeng Shi, *[a] Wenqing Liang,[a] Lintao Wang,[a] Sen Li,[a] Fei Zhang,[a] Zhuangzhuang Ma,[a] Yue Wang,[a] Yongzhi Tian,[a] Di Wu,[a] Xinjian Li,*[a] Yuantao Zhang,[b] Chongxin Shan[ac] and Xiaosheng Fang *[d]

Ultraviolet (UV) photodetectors with high spectrum selectivity are highly desired for certain special applications, like selected-wavelength imaging and UV-phototherapy. Here, for the first time, a highly stable and spectrum-selective self-powered UV photodetector based on lead-free $Cs_3Cu_2I_5$ films was demonstrated. By designing the $Cs_3Cu_2I_5$/GaN heterojunction, a narrow spectral response "window" of 300–370 nm was realized, and the working mechanism was investigated through the dependence of the spectral response on the absorber thickness and bias voltage. Because of the high material integrity of the $Cs_3Cu_2I_5$ films and competent interfacial charge transfer from $Cs_3Cu_2I_5$ to GaN, the proposed device exhibits a remarkable photodetection capability. Moreover, the proposed photodetector without encapsulation exhibits excellent working stability in ambient air, and typically it can operate continuously for more than 12 h under a high operation temperature of 373 K, indicating a high temperature tolerance and desired performance for practical applications under harsh environments. In addition, the device was used as the sensing pixels in a UV imaging system, and high-resolution imaging patterns were achieved. The results highlight the great potential of such lead-free $Cs_3Cu_2I_5$ as environment-friendly alternatives for stable and spectrum-selective UV photodetection without band-pass filters that can be employed in imaging.

New concepts

An intrinsically large light absorption coefficient, and high and well-balanced carrier transport ability endow metal-halide perovskites with great promise for high-performance photodetectors. However, compared to the intensive efforts on broadband photodetectors, narrowband photodetectors based on perovskites, especially targeting the ultraviolet (UV) region, have not been reported. Here, for the first time solution-processed lead-free $Cs_3Cu_2I_5$ films were used as the light absorber to fabricate spectrum-selective UV photodetectors by using the charge collection narrowing concept, overcoming the shortcomings of conventional strategies for making narrowband photodetectors (high cost, complex configuration, and difficult integration), and a narrow response "window" of 300–370 nm was achieved. Unlike traditional perovskites, lead-free $Cs_3Cu_2I_5$ is very stable against heat, UV light, and environmental oxygen/moisture. Typically, the unencapsulated device can endure a high working temperature (373 K) for 12 h continuous operation in ambient air. Further, UV imaging applications were demonstrated by deploying the photodetectors as sensing pixels. The results suggest that lead-free $Cs_3Cu_2I_5$ is potentially an attractive candidate for stable and narrowband UV photodetectors, rendering it potentially useful for the assembly of optoelectronic systems in the future.

Introduction

Ultraviolet (UV) photodetectors with high spectrum selectivity and small full-width at half-maximum (FWHM) are highly desired for some special applications, where detecting a specific wavelength while suppressing the background emission is required, like flame detection to explore the existence of a specific kind of chemical element, selected-wavelength imaging, fluorescence detection, defense and UV-phototherapy.[1–5] In general, narrowband detection can be achieved by combining broadband detectors with band-pass filters,[6–8] using narrowband absorption of photoactive materials,[9] or deliberately enhancing

[a] *Key Laboratory of Materials Physics of Ministry of Education, Department of Physics and Engineering, Zhengzhou University, Daxue Road 75, Zhengzhou 450052, China. E-mail: shizf@zzu.edu.cn, lixj@zzu.edu.cn*
[b] *State Key Laboratory on Integrated Optoelectronics, College of Electronic Science and Engineering, Jilin University, Qianjin Street 2699, Changchun 130012, China*
[c] *State Key Laboratory of Luminescence and Applications, Changchun Institute of Optics Fine Mechanics and Physics, Chinese Academy of Sciences, Changchun 130033, China*
[d] *Department of Materials Science, Fudan University, Shanghai 200433, China. E-mail: xshfang@fudan.edu.cn*

† Electronic supplementary information (ESI) available: EDS, XPS, and transmission spectra of the $Cs_3Cu_2I_5$ films, absorption of the $Cs_3Cu_2I_5$ films, GaN layer, and the $Cs_3Cu_2I_5$/GaN hybrid, temperature-dependent PL decay curves, heating/cooling cycling PL measurements, thermogravimetric data, photostability, and UPS of the $Cs_3Cu_2I_5$ films, confirmation of the Ohmic contacts between the semiconductors and metal, stability and noise current of the photodetector, high-frequency test of the device at zero bias, morphology, structural, and optical properties of the $Cs_3Cu_2I_5$ films before and after heating treatment, confirmation of the recoverability of the photocurrent after the aging test, Table S1 fitting parameters of the PL decay curves, Table S2 electrical properties of the $Cs_3Cu_2I_5$ films and GaN. See DOI: 10.1039/c9mh01371g

the absorption in a specific wavelength range through the plasmon effect.[10] For the first method, the design complexity of the photodetector systems is increased and the device is difficult to integrate, and the inherent limitations of filters including sensitivity to contamination, high cost, and surface scratches have to be considered. The second method is infeasible for a narrowband spectral response over a long-wavelength range. For the third method, it has a few problems, including high cost and complex configuration. Moreover, plasmon enhanced absorption cannot be adjusted over a large spectral range. Thus, there is a great need for low-cost narrowband photodetectors with architectural simplicity. In this regard, filter-free spectrum-selective photodetectors have recently attracted intense attention, for example, charge collection narrowing (CCN) with thick absorbing layers has been investigated for narrowband detection over a wide wavelength range, involving different kinds of materials.[11–15]

Recently, metal-halide perovskites have attracted huge attention due to their excellent optoelectronic features, including high light absorption coefficient, tunable emission wavelength, direct bandgap, and high and well-balanced carrier transport ability.[16–25] These properties make the materials an ideal candidate for optoelectronic devices. By developing such materials as the light absorber, much progress in broadband photodetectors has been witnessed in recent years.[26–30] In contrast, narrowband detectors based on perovskites materials have rarely been reported. In this connection, there are a few representative studies that deserve comments herein. For example, Huang *et al.* and Lin *et al.* demonstrated high-performance narrowband photodetectors with a tunable spectral response by using methylammonium lead trihalide perovskite single crystals as the light absorber layer.[10,31] Similar photodetection behaviors were also reported in Kuang's and Zhang's studies.[32,33] In their cases, the success of bulk single crystal narrowband photodetection depends on the sharp change of the light absorption coefficient close to the band edge and surface-charge recombination, in other words, manipulation of the external quantum efficiency *via* CCN. In addition, by using two-dimensional (2D) perovskite single crystals, Li and coworkers successfully fabricated tunable narrowband photodetectors, and they attributed it to the self-trapped states in 2D perovskites and large conductivity in the out-of-plane direction.[34] Very recently, they reported a spectrum-selective dual-band photodetector based on centimeter-sized 2D layered perovskites, and the dual-band spectral response can be adjusted over the visible range by composition engineering.[35] Besides, by using all-inorganic $CsPbX_3$ (X = Cl/Br/I) polycrystalline thick films as the photoactive layer, Zeng and co-workers realized narrowband detection in the visual band and demonstrated the potential application in simulating the human visual system.[36] Despite the inspiring progress that has been made on perovskite narrowband photodetectors, the environmental instability and toxicity of conventional lead-halide perovskites has become a stumbling block that limits their further applications. Thus, exploring lead-free and environmentally stable perovskites to solve the above obstacles is urgent. Moreover, an indisputable fact is that the previously reported perovskite narrowband photodetectors always operate in the visible range, and there has been no relevant report targeted at the UV region as far as we know. Besides, in previous research on perovskite narrowband devices, the photodetector performance was mainly related to the responsivity, specific detectivity, external quantum efficiency, and other related parameters, but stability issues of the unencapsulated device were rarely investigated.

Following this line of thought, for the first time, a highly stable and spectrum-selective UV photodetector based on lead-free $Cs_3Cu_2I_5$ films was demonstrated. By using the CCN concept, the surface-charge recombination can be controlled through the thickness of the absorber and the device only responds to photons with an energy in a narrow "window" of 300–370 nm. The photodetectors demonstrate a high responsivity of 0.28 A W^{-1}, a specific detectivity of 1.4×10^{12} Jones, an on/off photocurrent ratio of 1.2×10^5, and fast response speeds of 95/130 μs (800 Hz) under UV light excitation (320 nm). Additionally, the device without encapsulation exhibits excellent working stability against thermal degradation in the open air, indicating a remarkable temperature tolerance and desired compatibility for applications under harsh conditions. Furthermore, we demonstrated high-resolution UV imaging applications based on the fabricated narrowband photodetectors. The results suggest that the present lead-free $Cs_3Cu_2I_5$ can serve as a good candidate for stable and spectrum-selective UV photodetection without band-pass filters.

Results and discussion

The morphology of the $Cs_3Cu_2I_5$ films on an n-GaN template was examined by scanning electron microscopy (SEM). As shown in Fig. 1a, the $Cs_3Cu_2I_5$ films were characterized by a dense morphology with a high surface coverage, and the mean grain size was about 330 nm. The energy dispersive X-ray spectroscopy (EDS) elemental mapping results (Fig. 1b) show that the Cs, Cu, and I elements are uniformly distributed over the selected square areas. The EDS spectrum quantitative analysis shown in Fig. S1 (ESI†) further confirmed that the atomic ratio of Cs : Cu : I is 3 : 1.98 : 5.22, close to the stoichiometry of the $Cs_3Cu_2I_5$ material. Fig. 1c shows typical X-ray diffraction (XRD) patterns of the as-grown samples in comparison with the XRD patterns of the standard $Cs_3Cu_2I_5$. A set of diffraction peaks at 24.11°, 24.86°, 25.68°, 26.40°, and 30.75° can be assigned to the (122), (400), (320), (222), and (004) planes of the orthorhombic $Cs_3Cu_2I_5$ (space group *Pnma*, a = 10.1743 Å, b = 11.6532 Å, c = 14.3621 Å, $\alpha = \beta = \gamma = 90°$). Moreover, X-ray photoelectron spectroscopy (XPS) measurements were performed to identify the valence state of Cu ions. As shown in Fig. S2 (ESI†), the binding energy at 932.2 and 951.9 eV can be assigned to Cu $2p_{3/2}$ and Cu $2p_{1/2}$, respectively, corresponding to the Cu (+1) state as reported in other studies.[37–40] In addition, the characteristic satellite peak of Cu^{2+} is reported at ~943 eV,[41] which is absent in our results. Therefore, the valence state of Cu in the products is +1, not divalent copper. Fig. 1d shows the schematic crystal structure of orthorhombic $Cs_3Cu_2I_5$, in which two types of Cu^+ sites were incorporated, a trigonal site and a tetrahedral site.

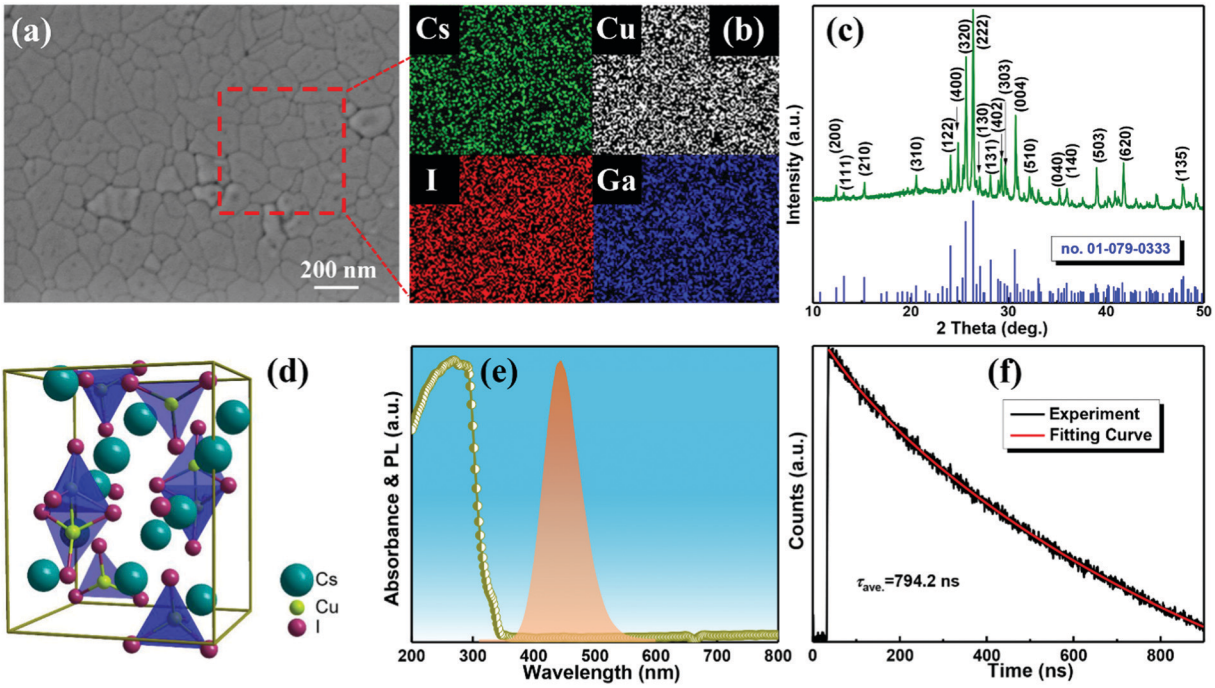

Fig. 1 (a) Top-view SEM images of the $Cs_3Cu_2I_5$ films. (b) EDS elemental mapping results for a selected region in (a). (c) XRD patterns (upper) of the as-grown $Cs_3Cu_2I_5$ films and the standard XRD patterns (bottom) for orthorhombic $Cs_3Cu_2I_5$. (d) Crystal structure of $Cs_3Cu_2I_5$. (e) Absorption and PL spectra of the $Cs_3Cu_2I_5$ films. (f) Time-resolved PL decay and fitting curve of the $Cs_3Cu_2I_5$ films.

Both of them form $[Cu_2I_5]^{3-}$ and each $[Cu_2I_5]^{3-}$ is separated by Cs^+ ions.[42] Preliminary optical studies (Fig. 1e) show that the $Cs_3Cu_2I_5$ films exhibit a strong and broad photoluminescence (PL) emission peak at 442 nm, and the FWHM is 70 nm. The corresponding absorption edge is at 326 nm. In addition, the $Cs_3Cu_2I_5$ films have high light transmission (>95%) in the visible spectral region, as shown in the measured transmission spectrum (Fig. S3, ESI†). Fig. S4 (ESI†) shows the absorption spectrum of the $Cs_3Cu_2I_5$ films grown on the GaN template, and two clear and steep absorption edges occur at ~326 and 365 nm, respectively, corresponding to the bandgap absorption of the upper $Cs_3Cu_2I_5$ and underlying GaN template. Note that a relatively large Stokes shift of ~116 nm implies that excited-state structural reorganization or exciton self-trapping is the possible transition mechanism of $Cs_3Cu_2I_5$.[42–44] In order to gain more information on the carrier recombination dynamics, we measured the PL decay of the $Cs_3Cu_2I_5$ films using transient-state PL measurements. As shown in Fig. 1f, the PL decay trace strictly fitted to a biexponential mode, producing an average lifetime of ~794.2 ns, and the detailed fitting parameters are listed in Table S1 (ESI†). Such a large carrier recombination lifetime allows longer time for collection and transport of photo-generated carriers, and is also an indicator of good photovoltaic performance for such materials. As deduced from previous research about copper-halide compounds, broad emission with a large lifetime is a feature of Cu(I)-complex phosphorescent emission involving Jahn–Teller distortion.[42,45,46] In detail, a Cu(I) halide with a d^{10} closed-shell favors a tetrahedral geometry. In the photoexcited state, Cu(I) with tetrahedral geometries forms a Jahn–Teller distorted Cu(II)-d^9 center.[42] In other words, the electronic configuration of Cu(I) $3d^{10}$ changes to Cu(II) $3d^9$ after the absorption of the bandgap photon energy, causing Jahn–Teller distortion and subsequent reorganization of the excited-state structure.

As we all know, the instability of conventional lead-halide perovskites is the main obstacle for their further applications in optoelectronic devices. Typically, lead-halide perovskites in moist air would decompose due to the hygroscopic amine salts, and even if the resulting materials and devices are dried again, the chemical reaction process is irreversible. In this study, the environmental stability of the $Cs_3Cu_2I_5$ films was tested by studying the effects of heat, UV light irradiation, and storage period on their optical and structural properties. Firstly, we performed thermal cycling PL tests at 293–373 K to evaluate the thermal stability of the $Cs_3Cu_2I_5$ films, and the results are shown in Fig. 2a–d. It can be observed that the relative PL intensity of the $Cs_3Cu_2I_5$ films gradually decreases with the increase of temperature (heating process) due to the added nonradiative recombination caused by the heating effect. To get a better understanding of this, PL decay measurements at different temperatures were performed. As shown in Fig. S5a (ESI†), the PL decay curve at 293 K can be fitted with a biexponential decay, and an average PL decay lifetime of 794.2 ns was obtained. Also, we observed that the PL lifetime depends strongly on the temperature. As summarized in Fig. S5b (ESI†), with the increase of temperature, the PL lifetime decreases gradually. As deduced from previous research, the decrease of the PL lifetime can be explained by the increase of charge-carrier trapping states as the relaxation pathway.[47,48] After the first cooling process was administered (Fig. 2a),

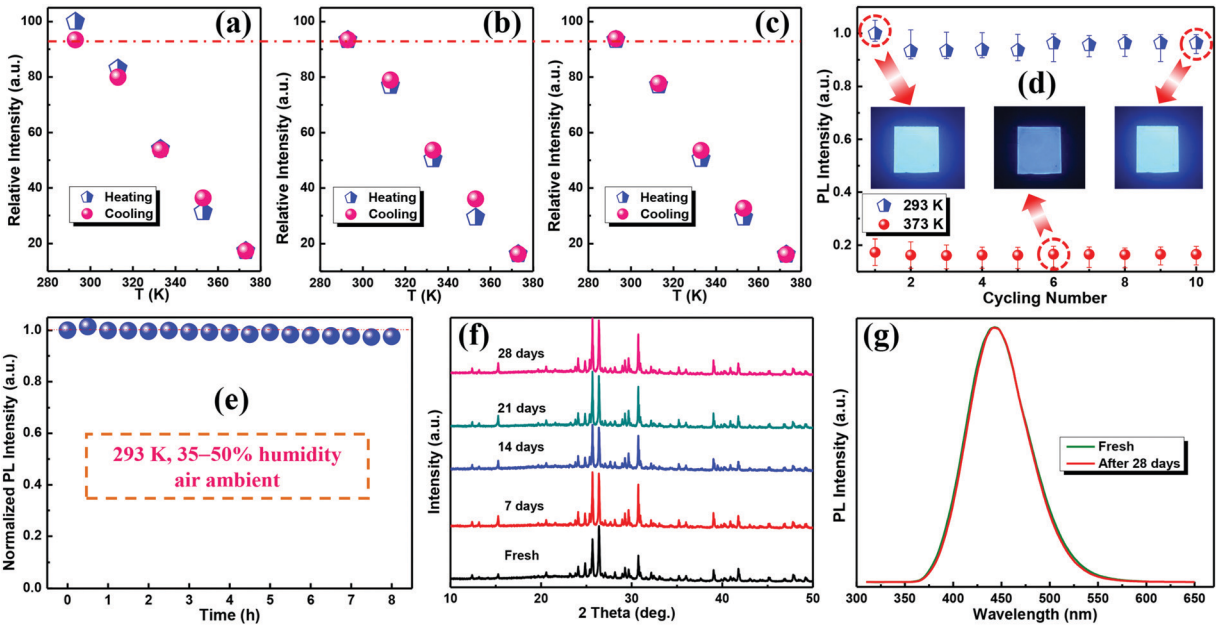

Fig. 2 (a–c) Three heating/cooling cycling PL measurements of the $Cs_3Cu_2I_5$ films. (d) The statistically integrated PL intensity of the $Cs_3Cu_2I_5$ films at two representative temperature points (293 and 373 K) over ten cycling measurements. The insets show the corresponding photographs of the films after different heating/cooling cycles under 265 nm light illumination. (e) Photostability test of the as-grown $Cs_3Cu_2I_5$ films under continuous UV light irradiation (265 nm, 3.0 mW cm^{-2}). (f) XRD, and (g) PL intensity evolution of the $Cs_3Cu_2I_5$ films after different storage periods in ambient air.

a small decay of about 6.6% was observed, much better than for conventional lead-halide perovskites.[49,50] The unrecoverable behavior may result from the added structural defects in the $Cs_3Cu_2I_5$ films due to the heating effect. Correspondingly, the radiative recombination probability of photo-generated carriers was reduced. More excitingly, over the subsequent two heating/cooling cycles, almost no significant emission decay occurs, as plotted in Fig. 2b and c. The insets of Fig. 2d display three representative photographs of the sample captured at cycle 1 (293 K), cycle 6 (373 K), and cycle 10 (293 K), from which the recoverable emission feature can be more intuitively observed. It should be mentioned that, in the ten heating/cooling cycles, the spectral shape and emission position did not change except for the change in peak intensity. Fig. S6 (ESI†) shows the corresponding PL spectra over the third cycle, and other cycles demonstrate the same phenomenon. We think that there are two main reasons for the better stability of $Cs_3Cu_2I_5$ films than that of conventional perovskites. On the one hand, $Cs_3Cu_2I_5$ has a 0D light-sensitive site of $[Cu_2I_5]^{3-}$, and low-dimensional perovskites generally exhibit better structural stability than the three-dimensional perovskite phase.[51] On the other hand, for conventional organic–inorganic hybrid perovskites ($CH_3NH_3PbX_3$), the $CH_3NH_3^+$ cation was extremely sensitive to oxygen and moisture. It has been reported that replacing methylammonium with inorganic cesium offers the perovskite extra thermal stability up to its melting at $\sim$500 °C,[52] but the decomposition enthalpy of $CsPbX_3$ is relatively low. Experimentally, thermogravimetric analysis of the $Cs_3Cu_2I_5$ films was conducted to measure the resistance of the material to high temperature. As shown in Fig. S7 (ESI†), the decomposition of the $Cs_3Cu_2I_5$ product starts at a temperature as high as 925 K, which is much higher than the decomposition temperature of 523 K for $CH_3NH_3PbBr_3$ and 853 K for $CsPbBr_3$.[53] Secondly, the photostability of the $Cs_3Cu_2I_5$ films was further tested under continuous UV light irradiation (265 nm, 3.0 mW cm^{-2}), and the PL spectra were extracted with a time interval of 0.5 h. As shown in Fig. 2e and Fig. S8 (ESI†), after continuous UV light irradiation for 8 h, a tiny decay of about 2% was generated with the FWHM and peak position of the PL spectra unchanged. The excellent stability of $Cs_3Cu_2I_5$ films against UV light degradation shows them to be a reliable light absorber for photodetection applications. Moreover, the environmental stability of the $Cs_3Cu_2I_5$ films, without any encapsulation and protection, was investigated by intermittently recording their XRD patterns and PL spectra after different storage periods. As shown in Fig. 2f, the as-grown $Cs_3Cu_2I_5$ films maintain the structural integrity without decomposition after 28-day storage in ambient conditions (20 °C, 35–50% humidity). In addition to a slight change of the peak intensity, no other diffraction signals appear, proving higher stability against oxygen and water degradation than conventional lead-halide perovskites. Also, the original emission performance can be almost retained after 28-day storage with the spectral shape unchanged, as shown in Fig. 2g. The results obtained demonstrate good stability of the $Cs_3Cu_2I_5$ films against heat, UV light, and environment oxygen/moisture, and are also evidence of a reliable $Cs_3Cu_2I_5$ photoactive material compatible for practical applications.

Fig. 3a shows the schematic structure of the $Cs_3Cu_2I_5$/GaN heterojunction photodetector, and the detailed preparation procedures can be found in the Experimental section. Based on the UV-visible absorption spectra and the UV photoelectron spectroscopy (UPS) data (Fig. S9, ESI†), the energy band alignment

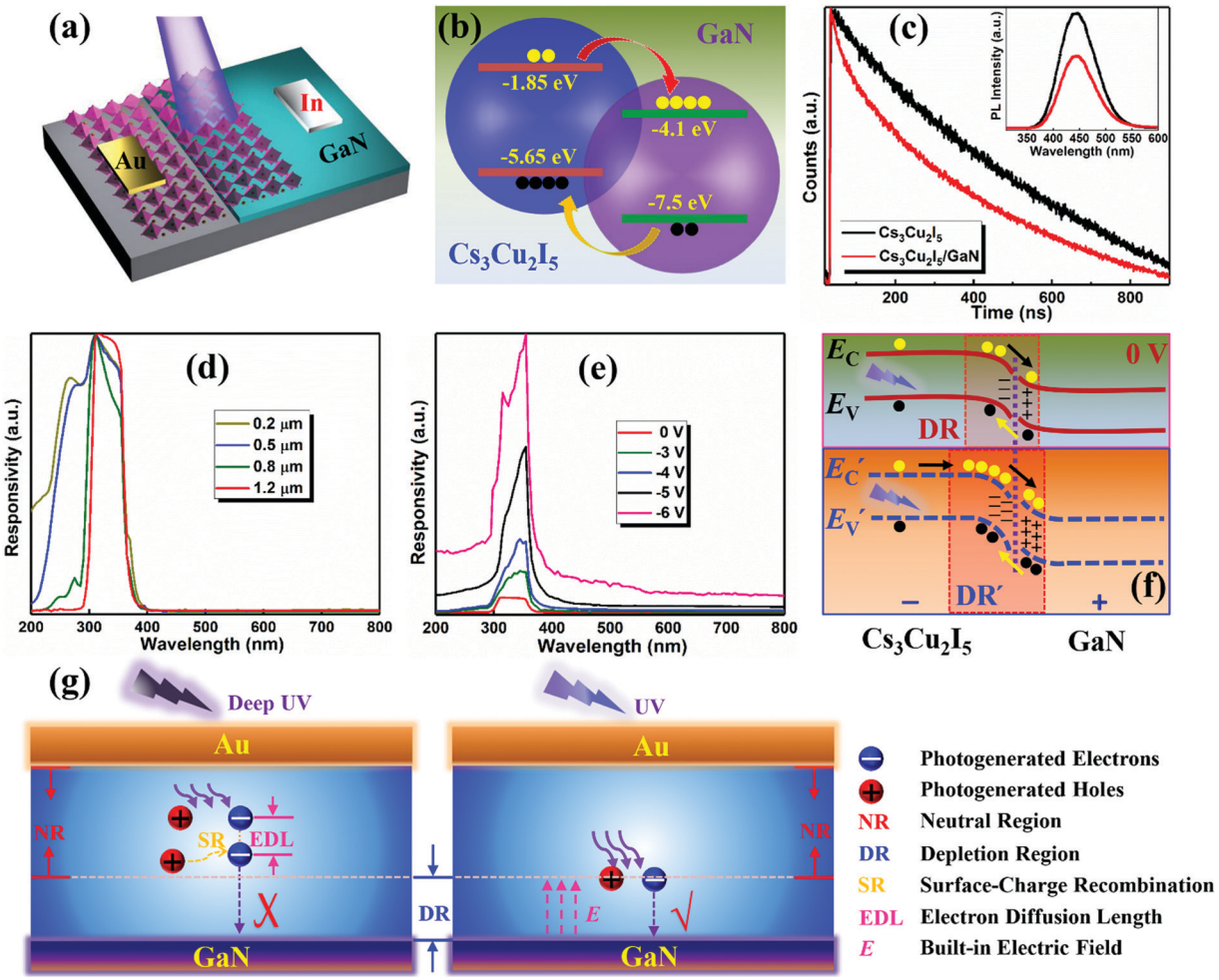

Fig. 3 (a) Schematic illustration of the $Cs_3Cu_2I_5$/GaN heterojunction device. (b) Energy band alignment of the $Cs_3Cu_2I_5$/GaN heterojunction. (c) PL spectra and PL decay curves of $Cs_3Cu_2I_5$ and the $Cs_3Cu_2I_5$/GaN hybrid with a thickness of 0.2 μm. Response spectra of the photodetector with (d) different absorber thicknesses, and (e) different bias voltages of the photodetector. (f) Energy band schematics of the $Cs_3Cu_2I_5$/GaN heterojunction under zero and negative bias. (g) The proposed mechanism for the surface-charge recombination assisted photodetector.

of the $Cs_3Cu_2I_5$/GaN heterojunction was drawn. Considering the fact that the $Cs_3Cu_2I_5$ films exhibit weak p-type conductivity properties with a hole concentration of about 4.3×10^{15} cm^{-3} (Table S2, ESI†), a p–n heterojunction can be established once the $Cs_3Cu_2I_5$ films and GaN are in contact, thus a built-in electric field would be formed at the hetero-interface because of the typical type-II band alignment, as seen in Fig. 3b. Once the photo-generated electron–hole pairs diffuse into the hetero-interface, they can be separated in opposite directions by the built-in electric field without an external power supply. The holes will transport to the perovskite side, whereas the electrons will move in the opposite direction, generating photocurrent in the external circuit. Moreover, the built-in electric field is capable of reducing the electron–hole recombination and preventing the electron transport from GaN to $Cs_3Cu_2I_5$, favoring a low reverse dark current and thus improving the detectivity. To support the above statement of charge carrier transfer at the hetero-interface, steady-state and transient-state PL spectra of $Cs_3Cu_2I_5$ and the $Cs_3Cu_2I_5$/GaN hybrid structure were therefore measured and put together for comparison. As shown in Fig. 3c, compared to the bare $Cs_3Cu_2I_5$ films, the integrated PL intensity of the $Cs_3Cu_2I_5$/GaN hybrid structure was reduced by ~39%, reflecting transfer of photo-generated carriers from $Cs_3Cu_2I_5$ to GaN. Meanwhile, the carrier lifetime of the $Cs_3Cu_2I_5$/GaN hybrid structure is reduced, indicating that the PL decay channel for the heterojunction device is faster, and it is also direct evidence of electron transfer behavior. Therefore, the GaN layer can be regarded as the electron-quenching layer. To study the performance of the photo-detector, we firstly examined the dependence of the photore-sponse on the incident light wavelength at zero bias. An interesting phenomenon was observed in which the spectral response of the photodetectors depends strongly on the thickness of the $Cs_3Cu_2I_5$ films. As shown in Fig. 3d, for the 0.2 μm-thickness $Cs_3Cu_2I_5$ films (canary-yellow line), a broad spectral response ranging from 200 to 370 nm was obtained, coinciding with the absorption of the $Cs_3Cu_2I_5$/GaN hybrid structure (Fig. S4, ESI†). By contrast, the responsivity in the short-wavelength range (200–300 nm) is relatively weaker than that in the long-wavelength range (300–370 nm), which may be due to the severe surface charge recombination (SR). For a better understanding of the

proposed mechanisms, added experiments were carried out by increasing the thickness of the $Cs_3Cu_2I_5$ films to different values. As seen in Fig. 3d, with the increase of the film thickness, the responsivity of the photodetectors in the short wavelength range starts to decrease, and finally disappeared into the baseline at a thickness of 1.2 μm, producing a desirable narrowband spectral response ranging from 300 to 370 nm. Note that this is the first report on a spectrum-selective UV photodetector based on lead-free perovskites as far as we know. The working mechanisms of the highly selective responsivity for the $Cs_3Cu_2I_5$/GaN heterojunction can be explained by Fig. 3g. In detail, the photoactive layer ($Cs_3Cu_2I_5$) of the photodetector can be divided into two regions: a depletion region (DR) near the GaN layer and a neutral region (NR) in the outer-layer near the Au electrode. As we all know, the absorption coefficient of the material increases as the incident wavelength decreases, and correspondingly the average light penetration depth is reduced. Therefore, for deep UV light excitation with a short penetration depth, a large amount of photo-generated carriers is generated in the NR close to the $Cs_3Cu_2I_5$ top surface and far away from the DR. They would be extinguished by the severe SR rather than being collected by the electrodes because of the limited electron diffusion length (EDL). As a result, the photo-generated carriers under deep UV light excitation cannot reach the DR, and are not capable of contributing to the photocurrent, making the photodetector highly spectrum-selective. For UV light excitation, the photons can penetrate deeper into the $Cs_3Cu_2I_5$ films because of the relatively smaller absorption coefficient and thus the photo-generated carriers are most likely to diffuse into the DR. With the aid of the built-in electric field (E) in the DR, the electron–hole pairs can be separated and collected rapidly. In this way, narrowband detection with the photon energy near the bandgap of $Cs_3Cu_2I_5$ can be achieved. The above observations indicate the "filter" effect of the outer-layer of the $Cs_3Cu_2I_5$ films. To depict the spectrum-selective feature of such photodetectors more clearly, bias-dependent responsivity spectra of the $Cs_3Cu_2I_5$/GaN heterojunction photodetector were measured. As shown in Fig. 3e, one can see that a negative bias can induce an obvious increase of the responsivity because of the enhanced charge extraction efficiency. An additional observation is that, with the increase of the reverse bias voltage, the responsivity in the short-wavelength range (200–300 nm) increases much more rapidly than that in the long-wavelength range (300–370 nm). Therefore, one conclusion can be made that the heterojunction photodetector will lose the narrowband detection ability under reverse bias (above −5 V). The above observation can be well understood by the fact that the applied negative bias shares the same direction as the E of the $Cs_3Cu_2I_5$/GaN heterojunction, giving rise to a higher electric field and a larger width of the DR. Thus, it is still possible that the photo-generated carriers under deep UV light excitation, even with a small light penetration depth, were quickly separated and collected in the time scale of their lifetime, contributing to the photocurrent. The above discussions on bias-dependent responsivity can be better unveiled by the energy band diagrams of the $Cs_3Cu_2I_5$/GaN heterojunction under zero and negative bias, as shown Fig. 3f.

Based on the rationale and working mechanisms outlined above, we selected 1.2 μm-thickness $Cs_3Cu_2I_5$ films to deliver a narrowband photodetector with a response between 300 and 370 nm. Fig. 4a shows the current–voltage (I–V) curves of the heterojunction photodetector under 320 nm UV illumination with varying light intensities (1 μW cm^{-2}–4.2 mW cm^{-2}). From the curves, it can be observed that there is a remarkable rectification feature with a rectification ratio over 10^6 (±3 V)

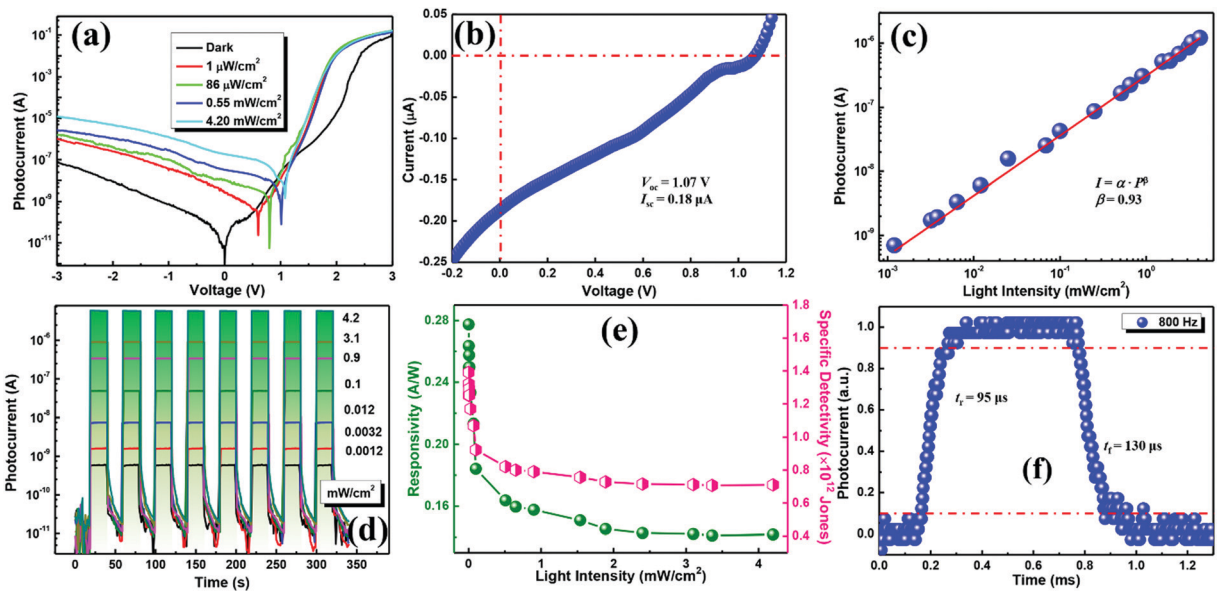

Fig. 4 (a) I–V curves of the photodetector tested in the dark and under different light irradiation intensity (320 nm). (b) Enlarged I–V curves showing the photovoltaic effect of the $Cs_3Cu_2I_5$/GaN heterojunction. (c) Logarithmic plot of the photocurrent *versus* light irradiation power at a bias of 0 V. (d) Photocurrent response measured under 320 nm light excitation with varying intensity at zero bias. (e) Responsivity and specific detectivity of the photodetector *versus* light intensity. (f) Rising and falling edges for estimating the rise time (t_r) and fall time (t_f) of the photodetector.

in the dark. Here, the rectification behavior was considered to result from the $Cs_3Cu_2I_5$/GaN heterojunction because of the established Ohmic contacts of Au/$Cs_3Cu_2I_5$/Au and In/GaN/In (Fig. S10, ESI†). In addition, one can see that both the photovoltage and photocurrent increased gradually with increasing light intensity because of the increased population of photogenerated carriers. Typically, the current of the device at zero bias greatly increases from 9.03×10^{-13} A in the dark to 1.86×10^{-7} A under UV light (4.2 mW cm^{-2}), and a short-circuit current (I_{sc}) of 0.18 μA and an open-circuit voltage (V_{oc}) of 1.07 V were obtained (Fig. 4b), manifesting a significant photovoltaic behavior and enabling the device to operate as a self-powered photodetector. Furthermore, the dependence of the photocurrent on the light intensity is shown in Fig. 4c. The data can be fitted well by the power law $I_P = \alpha \cdot P^{\beta}$, in which P is the light excitation power, α represents a proportional constant, and β is an empirical value that reflects the recombination of photoexcited carriers. The value of β is 0.93, close to that of an ideal photodetector ($\beta = 1$), which suggests a small recombination loss and the high quality of the $Cs_3Cu_2I_5$/GaN heterojunction. Fig. 4d shows the temporal photocurrent response of the device with different light intensity in self-powered mode. Apparently, the photocurrent increases gradually with the excitation intensity, and the heterojunction photodetector can be switched reversibly between the on and off states, yielding a maximum current on/off ratio of 1.2×10^5 (4.2 mW cm^{-2}). Even after 2000 cycles of operation, the photodetector can work well with high reproducibility and stability (Fig. S11, ESI†). Besides, it is worth noting that the on/off ratio of the photodetector can still reach 50 even under low light irradiation of 1.2 μW cm^{-2}, suggesting the capability to detect a weak signal. Based on the above data, the linear dynamic range (LDR) or photosensitivity linearity was estimated by using the expression[54–56]

$$\mathrm{LDR} = 20 \log \frac{I_p^*}{I_d} \quad (1)$$

in which I_p* represents the photocurrent obtained under 1.0 mW cm^{-2} light excitation, and I_d is the dark current. At zero bias, the LDR value was determined to be ~85 dB, better than the state-of-the-art commercial photodetectors.[25] Also, other device parameters, including the responsivity (R) and specific detectivity (D*), of the heterojunction photodetector were calculated based on the following formulas

$$R = (I_p - I_d)/P_{opt} \quad (2)$$

$$D^* = \frac{(A \cdot f)^{1/2}}{\mathrm{NEP}} \quad (3)$$

$$\mathrm{NEP} = (\overline{i_n^2})^{1/2}/R \quad (4)$$

in which I_p is the photocurrent, A represents the active area (0.008 cm^2), and P_{opt} is the intensity of incident light, f is the bandwidth (3500 Hz, as discussed later), NEP represents the noise equivalent power, and $\overline{i_n^2}^{1/2}$ is the noise current obtained by employing a lock-in amplifier at varying frequencies. Fig. S12 (ESI†) shows the curve of noise current *versus* frequency, and the noise level per unit bandwidth (1 Hz) was measured to be 0.53 pA Hz$^{-1/2}$. Consequently, R and D* were calculated to be 0.28 A W^{-1} and 1.4×10^{12} Jones (1 Jones = 1 cm Hz$^{1/2}$ W^{-1}), respectively, under 1 μW cm^{-2} light illumination at zero bias, which are comparable to many previously reported perovskite-based heterojunction photodetectors, as summarized in Table 1. Fig. 4e plots the calculated values of R and D* *versus* light intensity. Due to the increased carrier recombination probability at higher light intensity, both values present a declining trend with increasing light intensity, consistent with other reports.[57–59]

Further, the response speed of the $Cs_3Cu_2I_5$/GaN photodetector was measured to evaluate its capability to follow a varied optical signal. The schematic illustration is shown in Fig. S13a (ESI†), in which a waveform generator was used to produce the pulsed light (1 Hz to 8 kHz), and an oscilloscope was used to record the change of photocurrent with time. Fig. S13b–d (ESI†) display the photoresponse to pulsed light with different modulation frequencies, and the obtained data were normalized relative to the photoresponse tested under 1 Hz pulsed light. It can be seen that the photodetector can work with remarkable reproducibility in a wide frequency range. From the relative balance $(I_{max} - I_{min})/I_{max}$ shown in Fig. S13e (ESI†), a high 3dB frequency of ~3500 Hz was obtained, indicating that the $Cs_3Cu_2I_5$/GaN photodetector is able to monitor ultrafast optical signals. Further, the response speed of the device was assessed by analyzing the rising and falling edges of a single response cycle, as shown in Fig. 4f and Fig. S13f (ESI†). The response speeds were calculated to be 95/130 μs at 800 Hz and 32/43 μs at 5 kHz. It should be mentioned that the speed achieved is comparable to or faster than many studies on perovskite photodetectors.[61,62,67,68]

Table 1 Summary of the performance of heterojunction photodetectors

Device structure	Response range (nm)	Lead-free (yes/no)	Responsivity (A W^{-1})	D* ($\times 10^{12}$ Jones)	On/off ratio	Ref.
FTO/$MA_3Bi_2I_9$/Ag	380–900	Yes	0.002	1.3	—	60
TiO_2/$MAPbI_3$/spiro-OMeTAD	300–800	No	0.55	1	10^4	61
ITO/$CsPbBr_3$–ZnO NPs/Ag	400–530	No	0.0115	—	12.86	62
Graphene/$(PEA)_2SnI_4$/MoS_2/graphene	400–700	Yes	0.121	0.008	—	63
In/GaN/$Cs_2AgBiBr_6$/Au	200–550	Yes	1.46	9.4	10^4	64
ITO/SnO_2/$Cs_2AgBiBr_6$/Au	300–520	Yes	0.11	0.024	—	65
Au/spiro-OMeTAD/$CsPbBr_3$/SnO_2/ITO	300–550	No	0.172	4.8	1.3×10^5	66
$CsPbX_3$/α-Si radial junction	300–700	No	0.054	—	2.1×10^3	67
Au/MoS_2–$CsPbBr_3$/Au	350–550	No	4.4	0.025	10^4	68
In/GaN–$Cs_3Cu_2I_5$/Au	300–370	Yes	0.28	1.4	1.2×10^5	This work

As mentioned above, such lead-free $Cs_3Cu_2I_5$ films demonstrated remarkable material stability against heat, UV light, and environment moisture/oxygen degradation (Fig. 2). For real application in the photodetection field, research on the working stability of such heterojunction devices is highly necessary and desired to be conducted. In the present case, we firstly examined the long-term operation stability of the unencapsulated device at four temperature points (293, 333, 353, and 373 K) in ambient air (35–50% humidity), in which a zero bias and an excitation intensity of 0.90 mW cm^{-2} were fixed and the photocurrent was recorded in real time. It can be seen in Fig. 5a that the photocurrent at 293 K shows an increasing trend over the whole period (12 h). This may be due to the "photoactivation" behavior as observed in previous studies.[69] Generally, after continuous running for a long time, the temperature of the working area would increase. On the one hand, the raised temperature favors the separation of electrons and holes. On the other hand, the increased charge carrier density at high temperature could reduce the effective energy barrier height. Both factors favor easier carrier transport and contribute to an increase in photoconductivity. The same situation also happens at 333 K. As presented in Fig. 5b, the photocurrent displays an increasing trend in the first 7 h and then shows a reducing trend in the last 5 h. Therefore, we speculate that the negative role of temperature also exists at such a temperature level, and the undesired heating effect has to be considered at this moment. As the temperature was further increased to 353 and 373 K, obvious photocurrent decay of ~8.9% and 10% occurred over 12 h continuous running, as shown in Fig. 5c and d. Even so, the device stability in our work is still better than that in other studies.[70,71] Note that the photocurrent decay can be attributed to the added trap states induced by the heating effect, by which the photo-generated carriers could be trapped with a certain probability and cause the decay of the photocurrent. Further, we evaluated the thermal stability of the $Cs_3Cu_2I_5$/GaN heterojunction photodetector over a longer running time, and the responsivity of the device was intermittently collected at 373 K in ambient air. As shown in Fig. 5e, a very slow declining rate of responsivity can be distinguished and about a 10% decay occurs after a 300 h aging test. The above results suggest that the photocurrent decay or photo-generated carrier

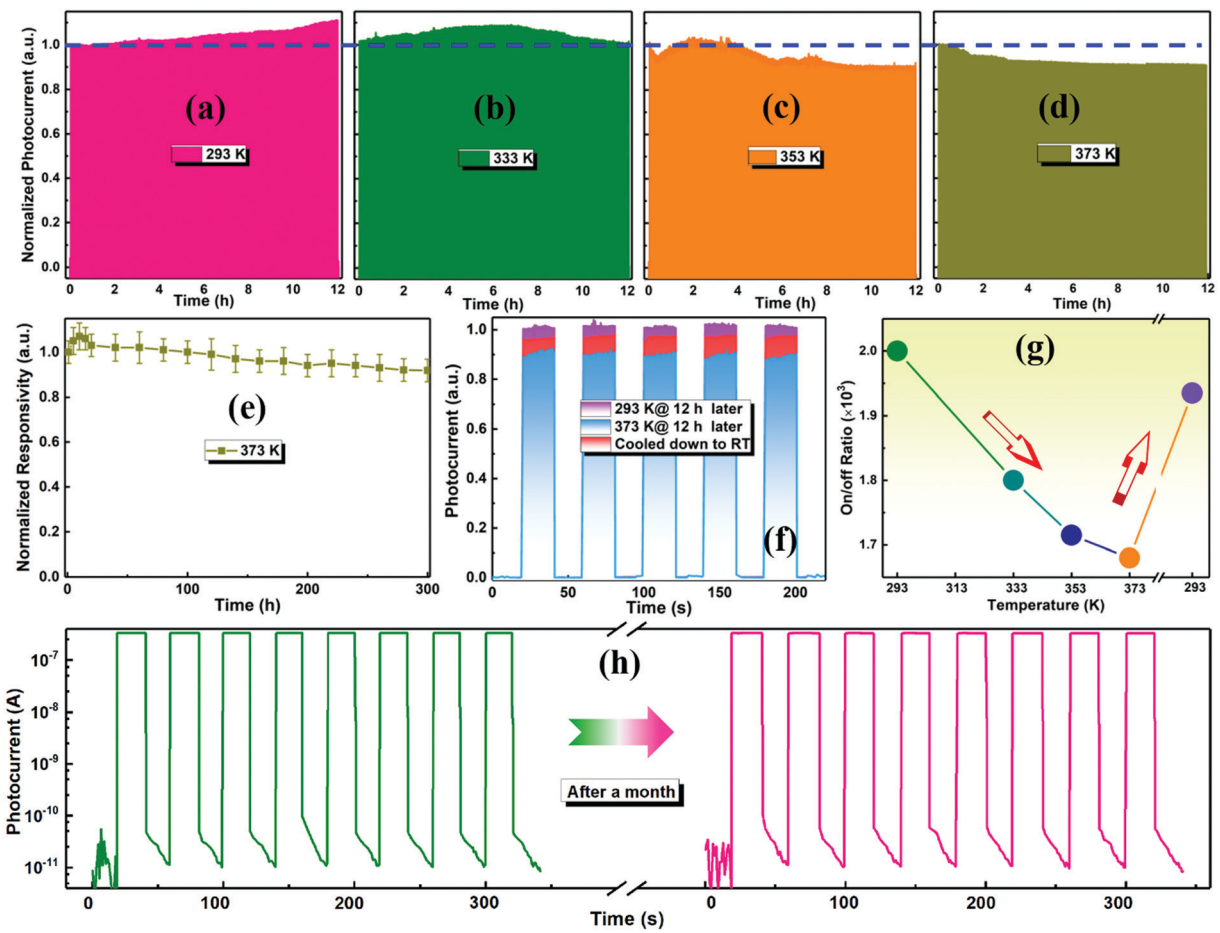

Fig. 5 Normalized photocurrent of the unencapsulated heterojunction photodetector *versus* running time at (a) 293 K, (b) 333 K, (c) 353 K, and (d) 373 K. The light intensity is fixed at 0.9 mW cm^{-2}. (e) Responsivity evolution of the heterojunction photodetector monitored at 373 K in ambient air. (f) Temporal photoresponse curves of the device after aging for 12 h at 293 and 373 K, and after naturally cooling to 293 K. (g) One thermal cycling measurement of the device revealing its variation of the on/off photocurrent ratio at different temperatures. (h) Long-term storage stability of the photodetector in ambient air. The last eight cycles are the photoresponse after storage for 1 month.

trapping does not increase in proportion with the running time, or the heat resistance of such a heterojunction device enables one to balance the accumulation of the heating effect with time. Most likely, such a good heat resistance ability of the $Cs_3Cu_2I_5$/GaN heterojunction benefits from a rational device design with an all-inorganic structure. In addition, it is worth noting that the photocurrent decay at high temperature is recoverable when the device is cooled down to room temperature (RT). Fig. 5f shows the temporal photoresponse curves of the device after running for 12 h at 293 and 373 K, respectively, and the reduced photocurrent at 373 K is consistent with the above results. Meanwhile, after the photodetector was cooled down to RT, the photocurrent could recover to 97% of the original level, demonstrating the recoverability and excellent temperature tolerance of the photodetector, and making the practical applications of such devices a real possibility. Since such a temperature level is not sufficient to cause a chemical reaction or phase transition in the $Cs_3Cu_2I_5$ films, the structural and optical properties of the materials can be well preserved, as seen in Fig. S14 (ESI†). Therefore, once the working device was naturally cooled down to RT, the trap states in the $Cs_3Cu_2I_5$ films will reduce remarkably, but could not recover to the initial level. Moreover, we observed that the recoverability of the photocurrent depends strongly on the working temperature. As shown in Fig. S15a (ESI†), for the aging test at 353 K, the photocurrent of the device can recover to 100% of the original level, while, for the aging test at 393 K (Fig. S15b, ESI†), the photocurrent of the device can recover to 90% of the original level. The results suggest that the cooling down process (back to 293 K) could not remove the trap states absolutely, especially at higher temperature. According to the temperature-dependent photocurrent–time curves, the on/off photocurrent ratios at four temperature points were calculated and are summarized in Fig. 5g. Obviously, the on/off photocurrent ratio decreases with increasing temperature under the same test conditions and at 373 K the on/off photocurrent ratio is reduced by 16%, while, after the working device is naturally cooled down to 293 K, the on/off ratio could almost recover to its original value. More excitingly, the present device, without any encapsulation and protection, can work efficiently after one-month storage in the open air, and maintain almost the same photocurrent under the same test conditions (320 nm, 0.9 mW cm^{-2}), as presented in Fig. 5h. The excellent storage stability achieved above is superior to the performance of organic–inorganic hybrid perovskite-based devices.[70,72] The above observations suggest that the studied heterojunction photodetector has stable and reproducible characteristics, as well as good temperature resistance, rendering it potentially useful for the assembly of optoelectronic systems in the future.

To assess the capability of the photodetector for recording image information, which is very important in optical fields such as fax machines and cameras, a UV imaging system was constructed by using the heterojunction photodetector as sensing pixels. Fig. 6a displays the schematic illustration of the measurement setup, in which a photo-mask with a hollow pattern was put between the laser illumination and the device, and the photo-mask can be moved in horizontal and vertical direction (x–y direction) by a 2D translation stage controlled by a software-programmed computer. In the working process, the laser beam passed through the photo-mask and irradiated the photodetector; the current signals from the heterojunction device and the corresponding position coordinates of the photo-mask were recorded in real time by a lock-in amplifier and a computer simultaneously, which could be transformed to a current mapping pattern. Note that the measured dark current and photocurrent respectively represent the background noise level and light intensity level at each pixel, inducing the dark and bright contrast in the imaging patterns. Fig. 6b shows the high-resolution imaging results under 325 nm light illumination, including the abbreviation of the hollow ultraviolet logo "UV" and a solid symbol of a deer. It can be seen that the two images were clearly resolved and well consistent with the photo-mask in shape, implying the high fidelity features of the imaging system and the reliable imaging function of the device.

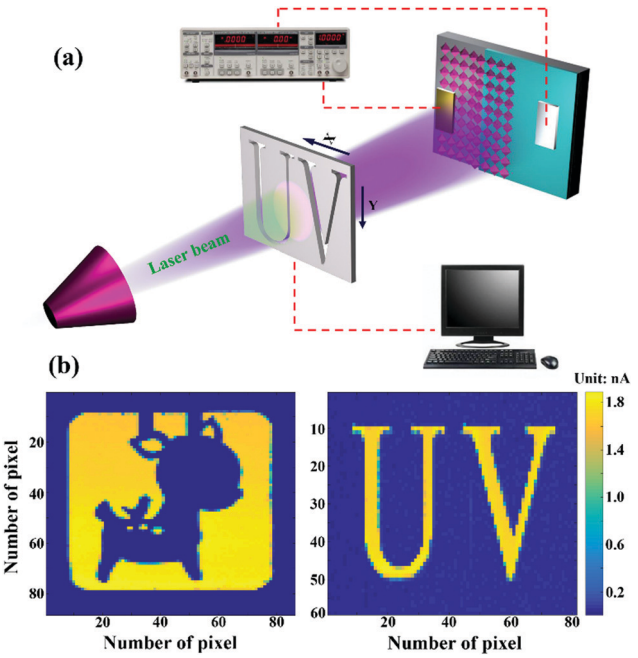

Fig. 6 (a) Schematic illustration of the experimental setup for the image sensing application of the studied heterojunction photodetector. (b) The corresponding current mapping of deer and UV patterns.

Conclusions

In conclusion, we have demonstrated a highly-stable and spectrum-selective self-powered UV photodetector based on solution-processed lead-free $Cs_3Cu_2I_5$ films by using the CCN concept. The device only responds to photons with an energy in a narrow "window" of 300–370 nm, and we investigated its working mechanism through the dependence of the spectral response on the absorber thickness and bias voltage. In addition to excellent photodetection performance, the proposed photodetector without encapsulation also demonstrates good operation stability in ambient air. Typically, it can endure a high operation

temperature of 373 K for 12 h continuous working; even after a month storage in the open air, the photodetector can function properly and its photodetection capability can almost be retained, which indicates a good temperature tolerance and desired compatibility for practical applications under harsh conditions. Further, with the help of an optically-assisted displacement platform, the hybrid heterojunction detector performed as the sensing pixels in a UV imaging system. The results obtained above may promise stable and spectrum-selective UV photodetection based on such lead-free $Cs_3Cu_2I_5$ materials, and the simple device structure will show great potential for hybrid optoelectronic systems.

Experimental section

In this work, commercially available n-GaN/Al_2O_3 templates were used as substrates, which were ultrasonically cleaned with ethanol, acetone, and deionized water for 10 min, respectively. Next, the template was treated with Ar gas plasma for 15 min. The GaN layer was $\sim$3.0 μm in thickness and showed n-type conductivity with a carrier concentration of 5.9×10^{18} cm^{-3} and a carrier mobility of 352 cm^2 V^{-1} s^{-1}. The $Cs_3Cu_2I_5$ films are prepared using solution processing *via* a one-step spin-coating method. In detail, the precursor solution mixed with 0.5 M CsI and 0.5 M CuI in dimethyl sulfoxide (completely dissolved at 75 °C) was spin-coated on the prepared substrate at 500 rpm for 10 s and then 2000 rpm for 30 s. The thickness of the films can be controlled by adjusting the speed and time of the spin-coating process. Following that, the sample was annealed at 100 °C for 1 h under N_2 conditions to evaporate the solvent and enhance the crystallization.

For device preparation, an In electrode ($\sim$100 nm) on GaN and a Au electrode ($\sim$20 nm) on the $Cs_3Cu_2I_5$ films were prepared by thermal evaporation by using a shadow mask and the heterojunction was established at the area where $Cs_3Cu_2I_5$ and GaN overlapped.

The morphology of the prepared $Cs_3Cu_2I_5$ films was tested by field-emission SEM (Jeol-7500F, 15 keV). XRD was conducted using a Panalytical X'Pert Pro. The PL spectra were recorded using a spectrofluorometer (Horiba; Fluorolog-3), and the transient-state PL measurement was conducted using a pulsed NanoLED (Horiba; 280 nm). The absorption spectra were measured using a Shimadzu UV-3150 spectrophotometer. The electrical properties of the $Cs_3Cu_2I_5$ films and GaN layer were measured through Hall effect measurements (ACCENT HL5500PC, UK). The optoelectrical and electrical measurements were conducted by using a testing system that includes a monochromator, a digital SourceMeter (Keithley 2636B), an optical chopper (SRS, SR540), light sources, and an oscilloscope (Tektronix, DPO2012B) in air.

Conflicts of interest

There are no conflicts to declare.

Acknowledgements

This work was supported by the National Natural Science Foundation of China (No. 11774318 and 11604302), the Key Scientific Research Projects of Higher Education in Henan Province (18A140007), and the Support Program for Scientific and Technological Innovation Talents of Higher Education in Henan Province (19HASTIT017).

Notes and references

1 B. Aufiero, H. Talwar, C. Young, M. Krishnan, J. Hatfield, H. Lee, H. Wong, I. Hamzavi and G. Murakawa, *J. Photochem. Photobiol., B*, 2006, **82**, 132.
2 G. Wilson and R. DeFreez, *Proc. SPIE*, 2004, **5416**, 157.
3 F. Guo, B. Yang, Y. Yuan, Z. Xiao, Q. Dong, Y. Bi and J. Huang, *Nat. Nanotechnol.*, 2012, **7**, 798.
4 S. Nishiwaki, T. Nakamura, M. Hiramoto, T. Fujii and M. Suzuki, *Nat. Photonics*, 2013, **7**, 240.
5 H. Chen, K. Liu, L. Hu, A. Al-Ghamdi and X. Fang, *Mater. Today*, 2015, **18**, 493.
6 T. Xu, Y.-K. Wu, X. Luo and L. Guo, *Nat. Commun.*, 2010, **1**, 1.
7 S. Yokogawa, S. Burgos and H. Atwater, *Nano Lett.*, 2012, **12**, 4349.
8 Z. Li, S. Butun and K. Aydin, *ACS Photonics*, 2015, **2**, 183.
9 E. Cicek, R. McClintock, C. Cho and B. Rahnema, *Appl. Phys. Lett.*, 2013, **103**, 191108.
10 Y. Fang, Q. Dong, Y. Shao, Y. Yuan and J. Huang, *Nat. Photonics*, 2015, **9**, 679.
11 A. Armin, R. Jansen-van Vuuren, N. Kopidakis and P. Burn, *Nat. Commun.*, 2015, **6**, 6343.
12 P. Ni, C. Shan, S. Wang, X. Liu and D. Shen, *J. Mater. Chem. C*, 2013, **1**, 4445.
13 Y. Zhong, T. Sisto, B. Zhang, K. Miyata, X. Zhu, M. Steigerwald and F. Ng, *J. Am. Chem. Soc.*, 2017, **139**, 5644.
14 A. Solanki, S. Li, H. Park and K. Crozier, *ACS Photonics*, 2018, **5**, 520.
15 Q. Xiong, F. Chowdhury and X. Wang, *IEEE J. Sel. Top. Quantum Electron.*, 2018, **24**, 1900406.
16 Z. Shi, Y. Li, Y. Zhang, Y. Chen, X. Li, D. Wu, T. Xu, C. Shan and G. Du, *Nano Lett.*, 2017, **17**, 313.
17 N. Jeon, H. Na, E. Jung, T. Yang, Y. Lee, G. Kim, H. Shin, S. Seok, J. Lee and J. Seo, *Nat. Energy*, 2018, **3**, 682.
18 Q. Chen, H. Zhou, Z. Hong, S. Luo, H. Duan, H. Wang, Y. Liu, G. Li and Y. Yang, *J. Am. Chem. Soc.*, 2014, **136**, 622.
19 K. Ding, Y. Fang, S. Dong, H. Chen, B. Luo, K. Jiang, H. Gu, L. Fan, S. Liu, B. Hu and L. Wang, *Adv. Opt. Mater.*, 2018, **6**, 1800347.
20 T. Chiba, Y. Hayashi, H. Ebe, K. Hoshi, J. Sato, S. Sato, Y.-J. Pu, S. Ohisa and J. Kido, *Nat. Photonics*, 2018, **12**, 681.
21 C. Sun, Y. Zhang, C. Ruan, C. Yin, X. Wang, Y. Wang and W. Yu, *Adv. Mater.*, 2016, **28**, 10088.
22 F. Zhang, Z. Shi, Z. Ma, Y. Li, S. Li, D. Wu, T. Xu, X. Li, C. Shan and G. Du, *Nanoscale*, 2018, **10**, 20131.
23 S. Stranks, G. Eperon, G. Grancini, C. Menelaou, M. Alcocer, T. Leijtens, A. Herz, L. Petrozza and H. Snaith, *Science*, 2013, **342**, 341.

24 Y. Zhang, W. X. Xu, X. J. Xu, J. Cai, W. Yang and X. S. Fang, *J. Phys. Chem. Lett.*, 2019, **10**, 836.
25 Z. Shi, Y. Li, S. Li, X. Li, D. Wu, T. Xu, Y. Tian, Y. Chen, Y. Zhang, B. Zhang, C. Shan and G. Du, *Adv. Funct. Mater.*, 2018, **28**, 1707031.
26 B. Yang, F. Zhang, J. Chen, S. Yang, X. Xia, T. Pullerits, W. Deng and K. Han, *Adv. Mater.*, 2017, **29**, 1703758.
27 X. Li, D. Yu, J. Chen, Y. Wang, F. Cao, Y. Wei, Y. Wu, L. Wang, Y. Zhu, Z. Sun, J. Ji, Y. Shen, H. Sun and H. Zeng, *ACS Nano*, 2017, **11**, 2015.
28 Z. Zheng, F. Zhuge, Y. Wang, J. Zhang, L. Gan, X. Zhou, H. Li and T. Zhai, *Adv. Funct. Mater.*, 2017, **27**, 1703115.
29 W. Deng, L. Huang, X. Xu, X. Zhang, X. Jin, S. Lee and J. Jie, *Nano Lett.*, 2017, **17**, 2482.
30 Y. Li, Z. Shi, L. Lei, Z. Ma, F. Zhang, S. Li, D. Wu, T. T. Xu, X. Li, C. Shan and G. Du, *ACS Photonics*, 2018, **5**, 2524.
31 Q. Lin, A. Armin, P. Burn and P. Meredith, *Nat. Photonics*, 2015, **9**, 687.
32 H. Rao, W. Li, B. Chen, D. Kuang and C. Su, *Adv. Mater.*, 2017, **29**, 1602639.
33 L. Li, Y. Deng, C. Bao, Y. Fang, H. Wei, S. Tang, F. Zhang and J. Huang, *Adv. Opt. Mater.*, 2017, **5**, 1700672.
34 J. Li, J. Wang, J. Ma, H. Shen, L. Li, X. Duan and D. Li, *Nat. Commun.*, 2019, **10**, 806.
35 J. Wang, J. Li, S. Lan, C. Fang, H. Shen, Q. Xiong and D. Li, *ACS Nano*, 2019, **13**, 5473.
36 J. Xue, Z. Zhu, X. Xu, Y. Gu, S. Wang, L. Xu, Y. Zou, J. Song, H. Zeng and Q. Chen, *Nano Lett.*, 2018, **18**, 7628.
37 K. Lu, Y. Lei, R. Qi, J. Liu, X. Yang, Z. Jia, R. Liu, Y. Xiang and Z. Zheng, *J. Mater. Chem. A*, 2017, **5**, 25211.
38 C. Bi, S. Wang, Q. Li, S. V. Kershaw, J. Tian and A. L. Rogach, *J. Phys. Chem. Lett.*, 2019, **10**, 943.
39 R. Roccanova, A. Yangui, H. Nhalil, H. Shi, M. Du and B. Saparov, *ACS Appl. Electron. Mater.*, 2019, **1**, 269.
40 T. Li, X. Mo, C. Peng, Q. Lu, C. Qi, X. Tao, Y. Ouyang and Y. Zhou, *Chem. Commun.*, 2019, **55**, 4554.
41 R. P. Vasquez, *Surf. Sci. Spectra*, 1993, **2**, 149.
42 T. Jun, K. Sim, S. Iimura, M. Sasase, H. Kamioka, J. Kim and H. Hosono, *Adv. Mater.*, 2018, **30**, 1804547.
43 Z. Yuan, C. Zhou, Y. Tian, Y. Shu, J. Messier, J. Wang, L. Van de Burgt, K. Kountouriotis, Y. Xin, E. Holt, K. Schanze, R. Clark, T. Siegrist and B. Ma, *Nat. Commun.*, 2017, **8**, 14051.
44 C. Zhou, Y. Tian, M. Wang, A. Rose, T. Besara, N. Doyle, Z. Yuan, J. Wang, R. Clark, Y. Hu, T. Siegrist, S. Lin and B. Ma, *Angew. Chem.*, 2017, **129**, 9146.
45 M. Halcrow, *Chem. Soc. Rev.*, 2013, **42**, 1784.
46 Y. Kim, J. Kim, J. Park, K. Park and Y. Lee, *Chem. Commun.*, 2017, **3**, 2858.
47 M. Jones, S. S. Lo and G. D. Scholes, *J. Phys. Chem. C*, 2009, **113**, 18632.
48 X. Wu, M. T. Trinh, D. Niesner, H. M. Zhu, Z. Norman, J. S. Owen, O. Yaffe, B. J. Kudisch and X. Y. Zhu, *J. Am. Chem. Soc.*, 2015, **137**, 2089.
49 Z. Shi, S. Li, Y. Li, H. Ji, X. Li, D. Wu, T. Xu, Y. Chen, Y. Tian, Y. Zhang, C. Shan and G. Du, *ACS Nano*, 2018, **12**, 1462.
50 S. Wei, Y. Yang, X. Kang, L. Wang, L. Huang and D. Pan, *Chem. Commun.*, 2016, **52**, 7265.
51 H. Tsai, W. Nie, J. Blancon, C. Stoumpos, C. Soe, J. Yoo, J. Crochet, S. Tretiak, J. Even and A. Sadhanala, *Adv. Mater.*, 2018, **30**, 1704217.
52 C. C. Stoumpos, C. D. Malliakas, J. A. Peters, Z. F. Liu, M. Sebastian, J. Im, T. Chasapis and A. C. Wibowo, *Cryst. Growth Des.*, 2013, **13**, 2722.
53 H. Cho, Y. Kim, C. Wolf, H. Lee and T. Lee, *Adv. Mater.*, 2018, **30**, 1704587.
54 X. Gong, Z. Tong, Y. Xia, W. Cai, J. Moon, Y. Cao, G. Yu, C. Shieh, B. Nilsson and A. Heeger, *Science*, 2009, **325**, 1665.
55 Y. Liu, Y. Zhang, K. Zhao, Z. Yang, J. Feng, X. Zhang, K. Wang, L. Meng, H. Ye, M. Li and S. Liu, *Adv. Mater.*, 2018, **30**, 1707314.
56 Y. Li, Z. Shi, X. Li and C. Shan, *Chin. Phys. B*, 2019, **28**, 017803.
57 C. Wu, Z. Wang, L. Liang, T. Gui, W. Zhong, R. Du, C. Xie, L. Wang and L. Luo, *Small*, 2019, **15**, 1900730.
58 B. Yang, F. Zhang, J. Chen, S. Yang, X. Xia, T. Pullerits, W. Deng and K. Han, *Adv. Mater.*, 2017, **29**, 1703758.
59 Y. Guo, C. Liu, H. Tanaka and E. Nakamura, *J. Phys. Chem. Lett.*, 2015, **6**, 535.
60 A. Hussain, A. Rana and M. Ranjan, *Nanoscale*, 2019, **11**, 1217.
61 G. Tong, X. Geng, Y. Yu, L. Yu, J. Xu, Y. Jiang, Y. Sheng, Y. Shi and K. Chen, *RSC Adv.*, 2017, **7**, 18224.
62 C. Li, C. Han, Y. Zhang, Z. Zang, M. Wang, X. Tang and J. Du, *Sol. Energy Mater. Sol. Cells*, 2017, **172**, 341.
63 C. Fang, H. Wang, Z. Shen, H. Shen, S. Wang, J. Ma, J. Wang, H. Luo and D. Li, *ACS Appl. Mater. Interfaces*, 2019, **11**, 8419.
64 Y. Li, Z. Shi, L. Lei, S. Li, D. Yang, D. Wu, T. Xu, Y. Zhi, Y. Lu, Y. Wang, L. Zhang, X. Li, Y. Zhang, G. Du and C. Shan, *Adv. Mater. Interfaces*, 2019, **6**, 1900188.
65 C. Wu, B. Du, W. Luo, Y. Liu, T. Li, D. Wang, X. Guo, H. Ting, Z. Fang, S. Wang, Z. Chen, Y. Chen and L. Xiao, *Adv. Opt. Mater.*, 2018, **6**, 1800811.
66 H. Zhou, J. Zeng, Z. Song, C. R. Grice, C. Chen, Z. Song, D. Zhao, H. Wang and Y. Yan, *J. Phys. Chem. Lett.*, 2018, **9**, 2043.
67 J. Lu, X. Sheng, G. Tong, Z. Yu, X. Sun, L. Yu, X. Xu, J. Wang, J. Xu, Y. Shi and K. Chen, *Adv. Mater.*, 2017, **29**, 1700400.
68 X. Song, X. Liu, D. Yu, C. Huo, J. Ji, X. Li, S. Zhang, Y. Zou, G. Zhu, Y. Wang, M. Wu, A. Xie and H. Zeng, *ACS Appl. Mater. Interfaces*, 2018, **10**, 2801.
69 M. Leng, Y. Yang, K. Zeng, Z. Chen, Z. Tan, S. Li, J. Li, B. Xu, D. Li, M. Hautzinger, Y. Fu, T. Zhai, L. Xu, G. Niu and J. Tang, *Adv. Funct. Mater.*, 2018, **28**, 1704446.
70 K. Aitola, K. Domanski, J. Baena, K. Sveinbjörnsson, M. Saliba, A. Abate, M. Grätzel, E. Kauppinen, E. Johansson, W. Tress, A. Hagfeldt and G. Boschloo, *Adv. Mater.*, 2017, **29**, 1606398.
71 Y. Li, Z. Shi, S. Li, L. Lei, H. Ji, D. Wu, T. Xu, Y. Tian and X. Li, *J. Mater. Chem. C*, 2017, **5**, 8355.
72 J. Yang, Q. Hong, Z. Yuan, R. Xu, X. Guo, S. Xiong, X. Liu, S. Braun, Y. Li, J. Tang, C. Duan, M. Fahlman and Q. Bao, *Adv. Opt. Mater.*, 2018, **6**, 1800262.

